Exciton states and oscillator strength in two vertically coupled InP/InGaP quantum discs

2004 J. Phys.: Condens. Matter 16 8633

(http://iopscience.iop.org/0953-8984/16/47/015)

INSTITUTE OF PHYSICS PUBLISHING JOURNAL OF PHYSICS: CONDENSED MATTER

J. Phys.: Condens. Matter **16** (2004) 8633–8652 PII: S0953-8984(04)84507-7

Exciton states and oscillator strength in two vertically coupled InP/InGaP quantum discs

M Tadić[1,2] **and F M Peeters**[1]

[1] Department of Physics, University of Antwerp (Campus Drie Eiken), Universiteitsplein 1, B-2610 Antwerp, Belgium
[2] Faculty of Electrical Engineering, University of Belgrade, PO Box 3554, 11120 Belgrade, Serbia

E-mail: Milan.Tadic@ua.ac.be and Francois.Peeters@ua.ac.be

Received 31 July 2004, in final form 25 October 2004
Published 12 November 2004
Online at stacks.iop.org/JPhysCM/16/8633
doi:10.1088/0953-8984/16/47/015

Abstract

Quantum mechanical coupling and strain in two vertically arranged InP/InGaP quantum dots is studied as a function of the size of the dots and the spacer thickness. The strain distribution is determined by the continuum mechanical model, while the single-band effective-mass equation and the multiband $\mathbf{k}\cdot\mathbf{p}$ theory are employed to compute the conduction and valence band energy levels, respectively. The exciton states are obtained from an exact diagonalization approach, and we also compute the oscillator strength for recombination. We found that the light holes are confined by strain to the spacer, which is the reason that the hole states exhibit coupling at much larger distances as compared with the electrons. At small d, the doublet structure of the hole energy levels arises as a consequence of the relocation of the light hole from the matrix to the regions located outside the stack, close to the dot–matrix interface. When d varies, the exciton ground state exhibits numerous anticrossings with other states, which are related to the changing spatial localization of the hole as a function of d. The oscillator strength of the exciton recombination is strongly reduced in a certain range of spacer thicknesses, which effectively turns a bright exciton state into a dark one. This effect is associated with anticrossings between exciton energy levels.

1. Introduction

The Stranski–Krastanov mode of epitaxial growth enables quantum dots to self-assemble in vertical stacks [1, 2], where the wavefunctions of the individual dots overlap as in molecules; therefore they are named *quantum-dot molecules* (QDMs). According to the simple view of coupling, the energy levels of two vertically coupled dots split into doublets, which are composed of bonding and antibonding counterparts. In order to model a quantum-dot device,

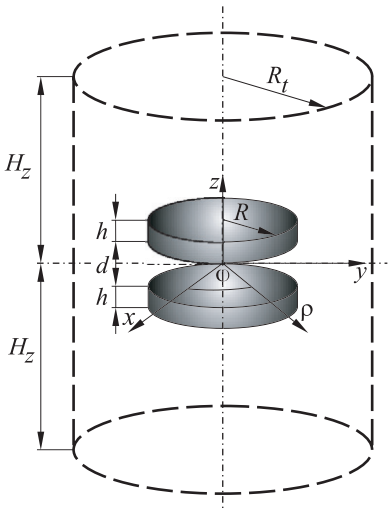

Figure 1. A sketch of a quantum-dot molecule (QDM) composed of two stacked InP dots (indicated by the dark areas) of radius R and thickness h, symmetrically arranged with respect to the $z = 0$ plane, and separated by an InGaP spacer of thickness d. The simulation area is given by the large (dashed) cylinder.

e.g. a laser, optical amplifier, or photonic detector, the coupling between electrons and holes should be properly accounted for. In addition to the band offset and effective masses, the size and shape of a quantum dot should be accurately known. However, the epitaxial growth technique has not reached a level which enables the fabrication of identical islands throughout the whole semiconductor matrix, and consequently there are substantial fluctuations in size and shape of the dots.

In contrast to the case for etched quantum-dot molecules, which are formed from lattice matched semiconductors, strain is inherently present in self-assembled quantum dots (SAQDs) [3, 4], which makes the requirements on modelling more demanding. In a previous paper [5] we showed that for single quantum dots (SQDs) the continuum mechanical (CM) model for strain captures the essential physics. Furthermore, this approach is most convenient when continuum models for the electronic structure are subsequently used. Indeed, we recently compared different models for cylindrical quantum dots, and found that the strain extracted from the CM model agrees favourably with the results from the valence force field model (using the Keating potential), and also with calculations based on Stillinger–Weber potentials [6]. In quantum dots based on low energy gap semiconductors, InAs for example, band mixing should also be taken into account, which leads one to adopt, e.g., the multiband $\mathbf{k} \cdot \mathbf{p}$ approach [7–9]. For the wide band-gap InP quantum dots embedded in a InGaP matrix, the six-band $\mathbf{k} \cdot \mathbf{p}$ model for the valence band states suffices, and the electron states are accurately described by a single-band model. A close comparison between the six-band and eight-band models does not reveal appreciable mixing between the valence and the conduction band states in InP/InGaP quantum dots. Another advantage of the six-band approach is that it does not suffer from spurious solutions, which are inherently present in the eight-band $\mathbf{k} \cdot \mathbf{p}$ model [10, 11].

Even the simple view that the strain in a quantum-dot molecule is built up from a superposition of the strains of the two dots separately indicates that the light holes are responsible for the hole coupling. In previous papers we showed that in a single quantum dot, the strain changes when the dot thickness varies, which leads to angular momentum transitions of the hole ground state [5, 6]. Similar changes are found here in QDMs, but now as a function of the spacer thickness.

In the present paper, we study the quantum-dot molecule composed of two InP quantum discs positioned one above the other and embedded in an InGaP matrix, as shown in figure 1.

Table 1. Envelope angular momenta (in units of $\hbar$) of the envelope functions in the $S^{\pm}_{+3/2}$, $S^{\pm}_{+1/2}$, and $P^{\pm}_{+5/2}$ states.

u_{n0}	$S^{\pm}_{+3/2}$	$S^{\pm}_{+1/2}$	$P^{\pm}_{+5/2}$
$\|3/2, 3/2\rangle$	0	−1	1
$\|3/2, 1/2\rangle$	1	0	2
$\|1/2, 1/2\rangle$	1	0	2
$\|3/2, -3/2\rangle$	3	2	4
$\|3/2, -1/2\rangle$	2	1	3
$\|1/2, -1/2\rangle$	2	1	3

For simplicity, we assume the same size for the two dots. The artificial molecule system is studied as a function of the spacer thickness and we investigate how energy levels split. The coupling due to strain is compared with the quantum mechanical coupling. Our theory is based on the CM model for the strain, the single-band effective-mass equation for the conduction band, and the six-band $\mathbf{k}\cdot\mathbf{p}$ Hamiltonian for the valence bands [5]. The spatial localization of the holes as a function of the spacer thickness is investigated, and the influence of the relocation of the electrons and holes due to the localization of an exciton is explored. The exciton states are obtained from an exact diagonalization calculation, where the products of the single electron and hole envelope functions are used as the basis. We exploit the multiband model, to find the dependence of the composition of the wavefunction on the spacer thickness, and also to ascertain how the optical activity of the exciton depends on the localization, and in turn on the distribution of strain.

In section 2, the model for computing the exciton states is described. The calculation of the exciton oscillator strength is explained in section 3. The numerical results are given in section 4. Section 5 contains our conclusions and the summary.

2. The model of exciton states

We assume that the quantum-dot molecule is composed of disc-shaped quantum dots and therefore the parity along the direction perpendicular to the two discs is a good quantum number in the axially symmetric approach to the electronic structure for both electrons and holes [12]. The single-particle states are determined following the procedure described in [5]. The electron states are labelled by nl^{σ}_{e}, where n denotes the principal quantum number, l_{e} is the orbital momentum of the electron, and σ is the parity of the state. Similarly, for the case of the hole states we use the symbol $nX^{\sigma}_{f_{\mathrm{h}}}$, where X denotes the lowest absolute value of the envelope angular momentum l_{h} for the six hole basis states, f_{h} is the total angular momentum of the hole in units of $\hbar$ ($F_{z\mathrm{h}} = f_{\mathrm{h}}\hbar$), and the other symbols have similar meanings to those for the electron case. For holes we find Kramers degeneracy with respect to reversal of both parity and total angular momentum. As an example, we give in table 1 the envelope angular momenta in the valence band (vb) states $S^{\pm}_{+3/2}$, $S^{\pm}_{+1/2}$, and $P^{\pm}_{+5/2}$, while the parities of the envelope functions in the even and odd states are given in table 2. The envelope functions are labelled by the periodic parts of the zone centre Bloch functions u_{n0} [5]. We refer further to the vb states as the hole states, keeping in mind that the Hamiltonian is written for the electrons in the valence bands, with the energy axis pointing from the valence bands upwards to the conduction band. When calculating exciton states, the phases of these envelope functions are appropriately taken into account [13].

The contribution of the different bands to the mixed hole state is given by

$$p_{\mathrm{vb}} = \int_{\Omega} (|F_i|^2 + |F_j|^2)\,\mathrm{d}\Omega, \tag{1}$$

Table 2. Parities of the envelope functions in the even ($X^{+}_{f_h}$) and odd ($X^{-}_{f_h}$) states.

u_{n0}	$X^{+}_{f_h}$	$X^{-}_{f_h}$
$\|3/2, 3/2\rangle$	+	−
$\|3/2, 1/2\rangle$	−	+
$\|1/2, 1/2\rangle$	−	+
$\|3/2, -3/2\rangle$	−	+
$\|3/2, -1/2\rangle$	+	−
$\|1/2, -1/2\rangle$	+	−

which is a measure of the coupling between the different hole states. In equation (1), vb is a symbol used for the hole band (with hh for heavy holes, lh for light holes, and so for the split-off band), while F_i and F_j denote the two envelope functions belonging to the specific band. Integration in equation (1) is performed over the domain ($\rho \leqslant R_t$, $|z| \leqslant H_z$), shown in figure 1.

Each function in the exciton envelope function spinor $F_{\mathrm{exc},s}$ is expanded in products of single-electron and single-hole wavefunctions,

$$F_{\mathrm{exc},s}(\mathbf{r}_\mathrm{e}, \mathbf{r}_\mathrm{h}) = \begin{bmatrix} F_{s,1} \\ F_{s,2} \\ F_{s,3} \\ F_{s,4} \\ F_{s,5} \\ F_{s,6} \end{bmatrix} = \sum_m \sum_n a_{mn} \begin{bmatrix} F_{\mathrm{h}m1} \\ F_{\mathrm{h}m2} \\ F_{\mathrm{h}m3} \\ F_{\mathrm{h}m4} \\ F_{\mathrm{h}m5} \\ F_{\mathrm{h}m6} \end{bmatrix} F_{\mathrm{e}n,s}, \tag{2}$$

which is written for the given electron spin s, a_{mn} are the coefficients of expansion, while $F_{\mathrm{e}n,s}$ and $F_{\mathrm{h}mi}$ are the single-electron and single-hole envelope functions. Expansion in equation (2) yields the secular equation

$$(E_{en} - E_{\mathrm{h}m} - E_{\mathrm{exc}})\delta_{im}\delta_{kn} + \sum_m \sum_n \sum_{j=1}^{6} \langle F_{\mathrm{h}ij} F_{\mathrm{e}k} | V_C | F_{\mathrm{h}mj} F_{en} \rangle = 0, \tag{3}$$

where E_{en} and $E_{\mathrm{h}m}$ denote the single-particle electron and hole energies and δ is the Kronecker symbol. Since all four envelope functions which are involved in the Coulomb matrix have a well defined parity, which is not removed by the Coulomb potential, each exciton state is formed from the single-electron and single-hole states of either equal parity or opposite parity, which will be named even and odd excitons, respectively. Hence, the exciton parity σ_{exc} is a good quantum number for the axially symmetric exciton, while the total angular momentum is composed of the angular momenta of the electron and the hole,

$$F_{z\mathrm{exc}} = (s + l_\mathrm{e})\hbar - F_{z\mathrm{h}}, \tag{4}$$

and is also conserved. Here, $s\hbar$ denotes the electron spin, which is included in the symbol of the exciton state, $nX^{\sigma_{\mathrm{exc}}}_{f_{\mathrm{exc}}s}$, where the meanings of the other symbols are similar to the ones for the holes case. Since $F_{z\mathrm{exc}}$ depends on the electron spin, the states with f_{exc} and $-f_{\mathrm{exc}}$ are not degenerate. But overall the exciton states have fourfold degeneracy, which arises from the double degeneracy of both the electron and the hole, and thus the exciton states are arranged in quartets. As demonstrated below, each quartet in the SQD splits into two quartets in the QDM composed of states of equal f_{exc} and s, but opposite parity. As an example,

$$Q^{-}_1 = [\, S^{-}_{-1\uparrow} \quad S^{+}_{+2\uparrow} \quad S^{+}_{+1\downarrow} \quad S^{-}_{-2\downarrow} \,], \tag{5}$$

is a quartet composed of the dark exciton states, but in the quartet

$$Q^{+}_1 = \big[\, \overline{S^{+}_{-1\uparrow(x,y)}} \quad S^{-}_{+2\uparrow} \quad \overline{S^{-}_{+1\downarrow(x,y)}} \quad S^{+}_{-2\downarrow} \,\big], \tag{6}$$

two states are optically active for x or y polarized light. In the following, states with a non-zero oscillator strength for exciton recombination are indicated by lines over the symbol of the state, with the subscript indicating the polarization of the absorbed light. The optical activity in Q_1^+ and Q_1^- is determined by the selection rules for the orbital momenta, and the selection rule for the parity, as elaborated above. The subscript 1 is chosen because $1Q_1^+$ is the ground state for all three values of the disc thickness. A higher energy is found for the Q_2^+ quartet:

$$Q_2^+ = [\, S^+_{0\uparrow} \quad S^-_{+1\uparrow} \quad S^+_{-1\downarrow} \quad S^-_{0\downarrow} \,], \tag{7}$$

which is dark, while the quartet

$$Q_2^- = [\, \overline{S^-_{0\uparrow(z)}} \quad \overline{S^+_{+1\uparrow(x,y)}} \quad \overline{S^-_{-1\downarrow(x,y)}} \quad \overline{S^+_{0\downarrow(z)}} \,] \tag{8}$$

contains excitons which are bright for arbitrary light polarization. However, population of the quartet $1Q_2^-$ in the single quantum dot is considerably reduced by its higher energy with respect to the $1Q_1^+$ quartet.

In order to explore the exciton localization, the six-dimensional space of the coordinates of the exciton is projected onto a two-dimensional one, by averaging the modulus squared of the exciton spinor at $\mathbf{r}_\mathrm{e} = \mathbf{r}_\mathrm{h} = \mathbf{r}$ over the polar angle:

$$|F_{\mathrm{exc},s}|^2_{\mathrm{2D}} = \frac{1}{2\pi}\int_0^{2\pi} F^\dagger_{\mathrm{exc},s}(\mathbf{r},\mathbf{r})\,F_{\mathrm{exc},s}(\mathbf{r},\mathbf{r})\,\mathrm{d}\varphi. \tag{9}$$

The subspace $\mathbf{r}_\mathrm{e} = \mathbf{r}_\mathrm{h} = \mathbf{r}$ is relevant for the oscillator strength of exciton recombination, and will be called the two-dimensional exciton probability density (2DPD). Also, the contributions of different hole bands in the exciton states are extracted from the exciton envelope functions $F_{s,i}$ and $F_{s,j}$, which belong to the band vb:

$$p_{\mathrm{vb,exc}} = \int_\Omega (|F_{s,i}(\mathbf{r},\mathbf{r})|^2 + |F_{s,j}(\mathbf{r},\mathbf{r})|^2)\,\mathrm{d}\Omega, \tag{10}$$

as in equation (1).

3. Oscillator strength

As a figure of merit for the recombination of an exciton, we use the oscillator strength,

$$f = \frac{2}{m_0 E_\mathrm{exc}}|M_\mathrm{exc}|^2, \tag{11}$$

where E_exc denotes the recombination energy, m_0 is the free-electron mass, and M_exc is the transition matrix element:

$$M_\mathrm{exc} = \int_{\mathbf{r}_\mathrm{e},\mathbf{r}_\mathrm{h}} \boldsymbol{\epsilon}\cdot\mathbf{p}_\mathrm{h}\tilde{\Psi}_\mathrm{exc}\,\mathrm{d}\mathbf{r}_\mathrm{e}\,\mathrm{d}\mathbf{r}_\mathrm{h}, \tag{12}$$

where the integration is performed over the electron and hole coordinates, $\boldsymbol{\epsilon}$ denotes the polarization vector, and $\tilde{\Psi}_\mathrm{exc}$ is the wavefunction composed of the vb electron envelope functions, which are directly extracted from our $\mathbf{k}\cdot\mathbf{p}$ Hamiltonian [5], and the conjugate complex of the cb electron envelope functions. $\mathbf{p}_\mathrm{h}$ acts only on the vb zone centre periodic parts of the Bloch functions. We compute M_exc by expanding it in the single-electron transition matrix elements:

$$M_\mathrm{exc} = \sum_m \sum_n a_{mn} M_{\mathrm{vc},mn}, \tag{13}$$

where $M_{\mathrm{vc},mn}$ denotes the transition matrix element connecting the m and n single-electron states in the valence and the conduction band, respectively. In the framework of the envelope

function approach, $M_{\mathrm{vc},mn}$ is resolved into the dipole matrix elements connecting the zone centre states, and the overlap integrals of the envelope functions:

$$M_{\mathrm{vc},mn} = \sum_{j=1}^{6} \langle S|\boldsymbol{\epsilon}\cdot\mathbf{p}_{\mathrm{h}}|u_j\rangle\langle F_{cn}|F_{vmj}\rangle. \tag{14}$$

The selection rule $\langle S|p_{\mathrm{h},\nu}|\nu'\rangle = (\mathrm{i}m_0P/\hbar)\delta_{\nu,\nu'}$, where ν denotes x, y, or z, and P is the Kane matrix element (taken to be equal in the dot and the matrix), applies to the envelope function overlap integrals. Therefore, overlaps between vb and cb envelope functions depend on the polarization of the incident light and the electron spin. For the hole Hamiltonian and the ordering of the zone centre states given in [5], the coupling coefficients are arranged in distinct sets:

$$(x,\uparrow): \quad \left[\tfrac{1}{\sqrt{2}},\ 0,\ 0,\ 0,\ \tfrac{1}{\sqrt{6}},\ \tfrac{1}{\sqrt{3}}\right] \tag{15a}$$

$$(x,\downarrow): \quad \left[0,\ \tfrac{1}{\sqrt{6}},\ \tfrac{1}{\sqrt{3}},\ -\tfrac{1}{\sqrt{2}},\ 0,\ 0\right] \tag{15b}$$

$$(y,\uparrow): \quad \left[\tfrac{\mathrm{i}}{\sqrt{2}},\ 0,\ 0,\ 0,\ -\tfrac{\mathrm{i}}{\sqrt{6}},\ -\tfrac{\mathrm{i}}{\sqrt{3}}\right] \tag{15c}$$

$$(y,\downarrow): \quad \left[0,\ \tfrac{\mathrm{i}}{\sqrt{6}},\ \tfrac{\mathrm{i}}{\sqrt{3}},\ \tfrac{\mathrm{i}}{\sqrt{2}},\ 0,\ 0\right] \tag{15d}$$

$$(z,\uparrow): \quad \left[0,\ -\tfrac{2}{\sqrt{6}},\ \tfrac{1}{\sqrt{3}},\ 0,\ 0,\ 0\right] \tag{15e}$$

$$(z,\downarrow): \quad \left[0,\ 0,\ 0,\ 0,\ \tfrac{2}{\sqrt{6}},\ -\tfrac{1}{\sqrt{3}}\right] \tag{15f}$$

where the electron spin and the polarization are explicitly declared in parentheses ahead of each coefficient set.

In the axially symmetric system, the envelope functions obey additional selection rules, which discard overlap integrals of envelope functions corresponding to different orbital momenta. For a given f_{h} of the vb electron, transitions to the cb states are only allowed if

$$f_{\mathrm{h}} - \tfrac{3}{2} \leqslant l_{\mathrm{e}} \leqslant f_{\mathrm{h}} + \tfrac{3}{2}. \tag{16}$$

Because of this rule, for example, $\mathrm{P}_{+5/2}$ vb states cannot transfer to the electron states in the s shell. The third restriction results from arguments based on parity, which prevents envelope functions of the opposite parity from forming finite overlap integrals. Since exciton states are composed of single-particle states, all three selection rules should affect the optical response of excitons as well.

4. Results and discussion

We apply our model to the InP/InGaP quantum-dot molecule, composed of two identical quantum discs, which have radius $R = 8$ nm, and we varied the thickness: $h = 2$, 3, and 4 nm. The thickness of the InGaP spacer d between the two vertically arranged discs is varied from 0 to 15 nm. The valence band offset was taken as -45 meV [7]; other parameters of InP and InGaP are given in table 1 of [5], except for the Kane energy, $E_P = 2m_0P^2/\hbar^2$, for which we took 20.7 eV for InP, as recently proposed in [14]. The strain distribution in the cylinder of radius $R_t = 30$ nm and height $2H_z = 80$ nm, shown in figure 1, was calculated. The same domain is used to expand the electron, hole, and exciton envelope functions. The single-particle envelope functions are expanded into products of 10 Bessel functions in the radial direction and 50 sine or cosine functions along the z coordinate. The choice of sine or cosine functions depends on the parity of the states and the symmetry of the matrix element in the Pikus–Bir Hamiltonian. For the exciton states, we select 320 pairs of electron and hole states with low values of the principal quantum number. The electron orbital momentum is limited to $|l_{\mathrm{e}}| < 2$, while $|f_{\mathrm{h}}| < 9/2$ for the hole.

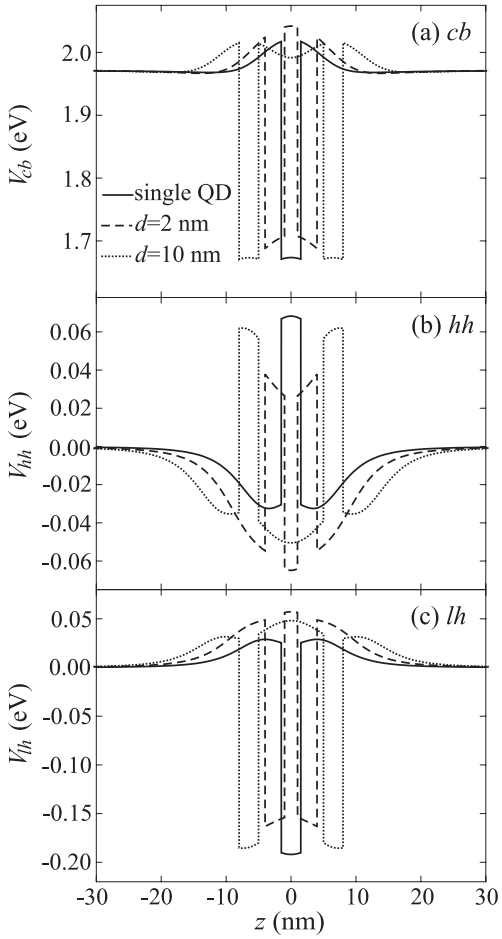

Figure 2. The effective potentials for the electrons (a), heavy holes (b), and light holes (c) in the SQD (solid curves) are compared with those in the QDM for a 2 nm (dashed curve) and for a 10 nm thick spacer (dotted curve) along the z axis. The dot radius equals 8 nm, the disc thickness is 3 nm, and the energy axis is oriented upwards in all bands.

4.1. Strain and effective potentials

The variations of the effective potentials in the conduction band, the heavy hole band, and the light hole band along the z coordinate in the QDM are shown in figures 2(a)–(c). One may note that for $d = 10$ nm, the hydrostatic strains within the individual dots are screened from each other (see figure 2(a)). For the 2 nm thick spacer, however, the cb effective potential inside the two dots acquires a triangular shape. Strain decreases the hh effective potential energies, when the inter-dot spacing decreases. For the light holes, however, the effective potential barriers inside the dots are decreased by the action of strain, while the regions formed inside the spacer and in the matrix near the base of the stack localize the light holes rather efficiently when d decreases.

The dot centre value of the cb effective potential is displayed in the upper portion of figure 3(a). For thin spacers, the maximum of the cb effective potential is located at $z = 0$, but when the dot separation increases, the $z = 0$ value decreases, and for the spacers as thick

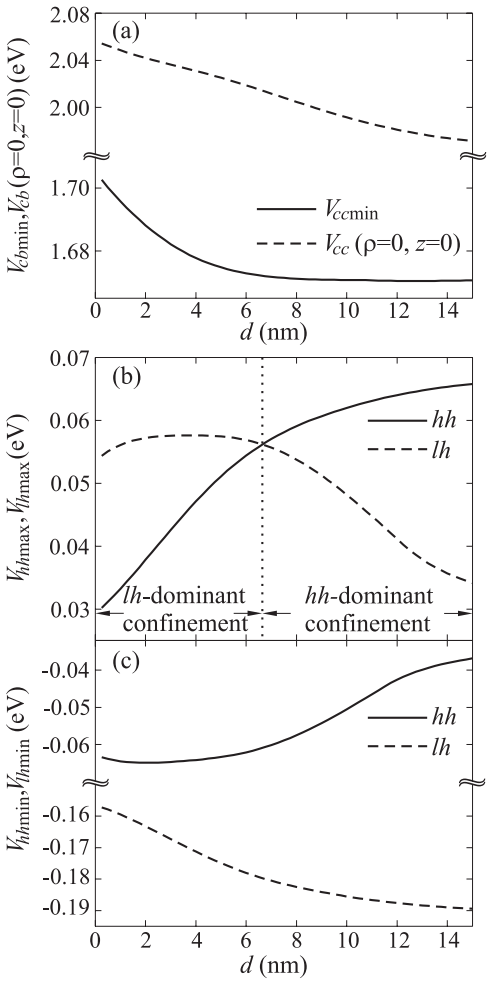

Figure 3. (a) The effective potential in the conduction band in the centre of the QDM, i.e. at ($\rho = 0, z = 0$), is shown by the dashed curve in the upper part, while the solid curve in the lower part displays the minimum of the same effective potential. (b) The maxima of the effective potentials in the QDM for the heavy holes (solid curve) and the light holes (dashed curve). The two curves cross, which indicates that holes in the ground state will have a dominant heavy (light) hole character for thick (thin) spacers. (c) The minima of the effective potentials for the heavy holes (solid curve) and the light holes (dashed curve) as they vary with the spacer thickness in the QDM. The dot thickness amounts to 3 nm.

as 10 nm shown in figure 2(a), it becomes lower than the value of the effective potential at the dot–matrix interface. The lowest value of the cb effective potential energy, also shown in figure 3(a), exhibits initially a steep decrease, but becomes almost flat for $d > 8.5$ nm, which implies that the hydrostatic strain inside one dot is completely screened from the strain in the other dot for large values of d. The vb extrema are depicted in figures 3(b) and (c). Note that the maxima of the hh and lh bands show opposite trends as a function of spacer thickness, which results in a crossing at 6.6 nm. Hence, for $d < 6.6$ nm one may anticipate dominant lh confinement, while in the opposite case, hh confinement may prevail. The minima of the hh and the lh bands, displayed in figure 3(c), vary such that the separation between them increases

from about 100 meV for thin spacers to more than 150 meV for thick spacers, which also enhances the hh character of the ground hole state when the spacer becomes thicker.

4.2. Electron and hole states

The electron energy levels in the QDM are ordered in doublet shells. The lowest energy doublets in the $s^{\pm}$, $p^{\pm}$, and $d^{\pm}$ shells are shown in figures 4(a)–(c), for $h = 2$, 3, and 4 nm, respectively. The shaded areas represent the energy continuum, and the thin horizontal lines in each shell represent the lowest SQD energy. The energy levels split into an even and odd state, but not symmetrically, with decreasing d. For a thick spacer, the energies of the ground states in all three shells increase above the levels in the SQD, and reach a local maximum at a certain value of $d = d_0$, called the coupling length, where the electron wavefunctions of the two dots start to overlap considerably, and therefore suppress the influence of the strain. A similar behaviour was demonstrated too in the QDMs of pyramid-shaped quantum dots [15], and for the vertical periodic arrangement of quantum dots [16]. But the physical explanation for this asymmetric behaviour was not provided in [15] and [16]. We find that d_0 depends on both l_e and h, but its value is in the range from 4 to 5 nm. Such small values indicate that quantum mechanical coupling in symmetrical self-assembled InP/InGaP QDMs is ineffective due to strain, except for rather small distances between the dots.

One may *a priori* infer that, similar to the case for electrons, the highest energy vb state is produced by f_h for which at least a single vb basis state has zero orbital momentum. This is possible in the $S^{\pm}_{\pm 3/2}$ and $S^{\pm}_{\pm 1/2}$ states, where the heavy holes and the light holes have zero orbital momentum, respectively. The ground state energies of these two symmetries were found to cross in the case of a SQD [5], as a function of the dot thickness, which is a consequence of the varying strain fields. A similar effect may occur in quantum-dot molecules, where the hh and lh effective potentials show opposite trends with the spacer thickness (see figure 3). This is demonstrated in figure 5 where crossings between states of the same parity and different angular momenta do indeed occur in the QDM, and are accompanied by crossings between states of the same angular momentum and different parity. The coupling in the $1S^{\pm}_{+3/2}$ states is established by the light holes, which become less confined as d decreases, yet, as figure 3(b) shows, even for $d = 15$ nm there is still a well sufficiently deep to localize the light holes.

The hole spatial localization depends on the spacer thickness. For large d, the energies of the $1S^{\pm}_{+1/2}$ and $1S^{\pm}_{+3/2}$ states increase when the spacer thickness decreases, which we refer to as regime I. After the maxima of the energies shown in figures 5(a) and (b) are reached, the hole localization enters regime II, where the confinement of the light holes in the spacer suppresses the confinement of the heavy holes inside the dots. The highest energy vb states of different angular momenta are close to each other in this range of d, and a situation arises where it is favourable for the $1P^{-}_{+5/2}$ state to become the ground state of the system, as shown in figures 5(c) and (d). Near $d = 3$ nm most of the anticrossings take place; these are followed by a considerable reconstruction of the hole wavefunctions, mainly from the spacer to the *effective quantum dots* for the light holes in the matrix. For spacers thinner than approximately 3 nm, all energy levels shown in figure 5 increase when d decreases, which we call regime III of hole localization, marked by a near degeneracy of states in the doublets. We noticed parity reversal in the ground state in this region.

The hole spectrum shown in figure 5 appears rather unusual and therefore we give in figure 6 a hand-waving picture to explain the dependence on d of the hole energies. The small d behaviour is due to the localization of the light holes in regions above and below the QDM. The vb energy decreases with increasing d because of a decrease of the confining potential (see figure 3(b)). There is a second branch which for small to intermediate values of d has

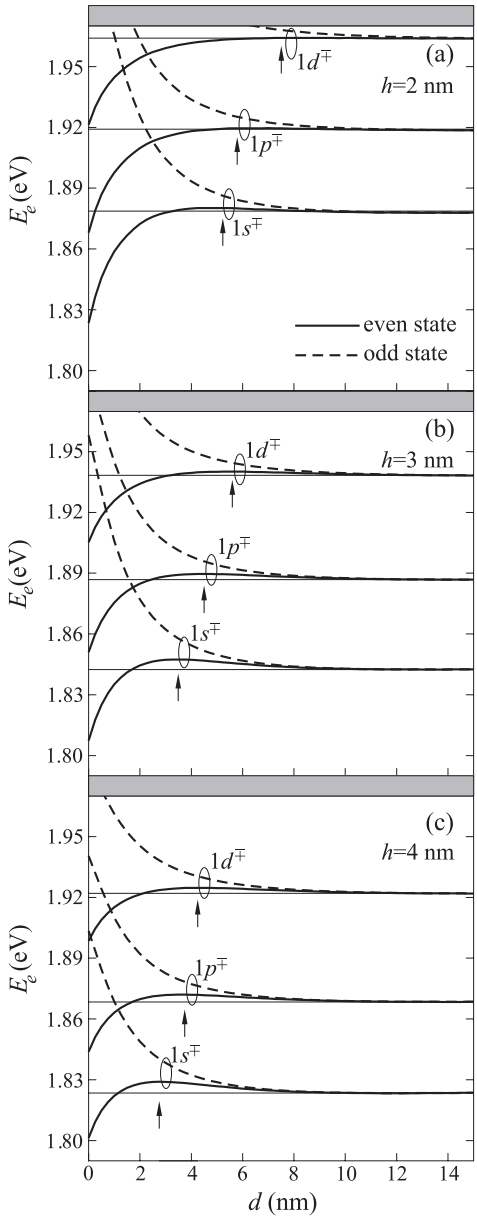

Figure 4. The spacer thickness dependence of the lowest electron energy doublets in the s, p, and d shells, for three quantum-dot thicknesses: (a) $h = 2$ nm, (b) $h = 3$ nm, and (c) $h = 4$ nm. The solid curves indicate even electron states, while the dashed curves are for the odd states. For thick spacers, strain suppresses electron coupling, which brings about upward shifts of the ground electron energy levels. The values of the coupling length are indicated by arrows. The continuum of the states in the QDM is shown by the shaded areas in the uppermost parts of the figures, and the same energy scale is adopted for all three values of h.

the opposite dependence on d. This state is mainly composed of the light holes localized between the two quantum dots; therefore their ground state energy increases (for the energy axis pointing upwards) with increasing d. Beyond a certain value of d the lowering of the

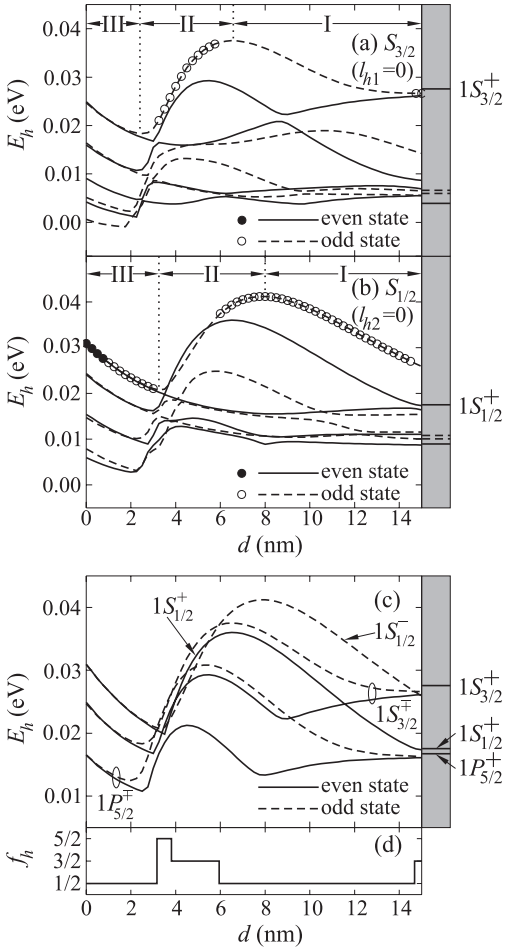

Figure 5. The hole energy levels in the QDM as a function of the spacer thickness: (a) $S_{+3/2}$, (b) $S_{+1/2}$, and (c) the highest energy vb states of $S_{+1/2}$, $S_{+3/2}$, and $P_{+5/2}$ symmetry. Solid curves indicate even hole states, and the dashed curves the odd hole levels. No two levels of the same parity cross. The energies in the SQD are shown by the appropriate curves in the shaded area. The ground state of the holes is denoted by solid dots (●) if it is even, and by open circles (○) if it is odd. (d) The z projection of the hole angular momentum in the ground state as it varies with the spacer thickness. The approximate borders between different regimes of the hole localization in the $1S^{-}_{+3/2}$ and $1S^{-}_{+1/2}$ vb states are indicated by the vertical dotted lines and are explicitly numbered. The ground SQD hole states are labelled on the right of the grey areas. The dot thickness equals 3 nm.

confining potential for the light holes between the dots starts to dominate, which leads to a lowering of the lh energy. The transition between these two levels leads to the anticrossings seen in figure 5 around 3 nm. This explanation is best suited for the $1S^{\pm}_{+1/2}$ states, where $l_{h2} = 0$, and may also be used to explain the dependence of the $1S^{\pm}_{+3/2}$ states for d less than about 10 nm. The lower energy vb levels in figure 5 vary similarly with d; therefore they can be approximately understood as excited versions of the previous ones.

In order to study the energy spectra of the holes more closely, we show in figure 7 the PDs of the $1S^{\pm}_{+3/2}$ and $2S^{\pm}_{+3/2}$ states for 3 nm thick quantum dots as they vary with the spacer

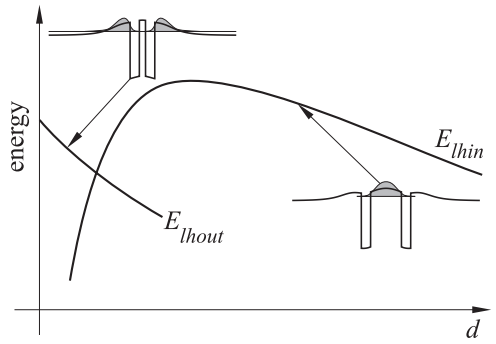

Figure 6. A schematic view of the dependence of the light hole localization in the QDM on the dot separation.

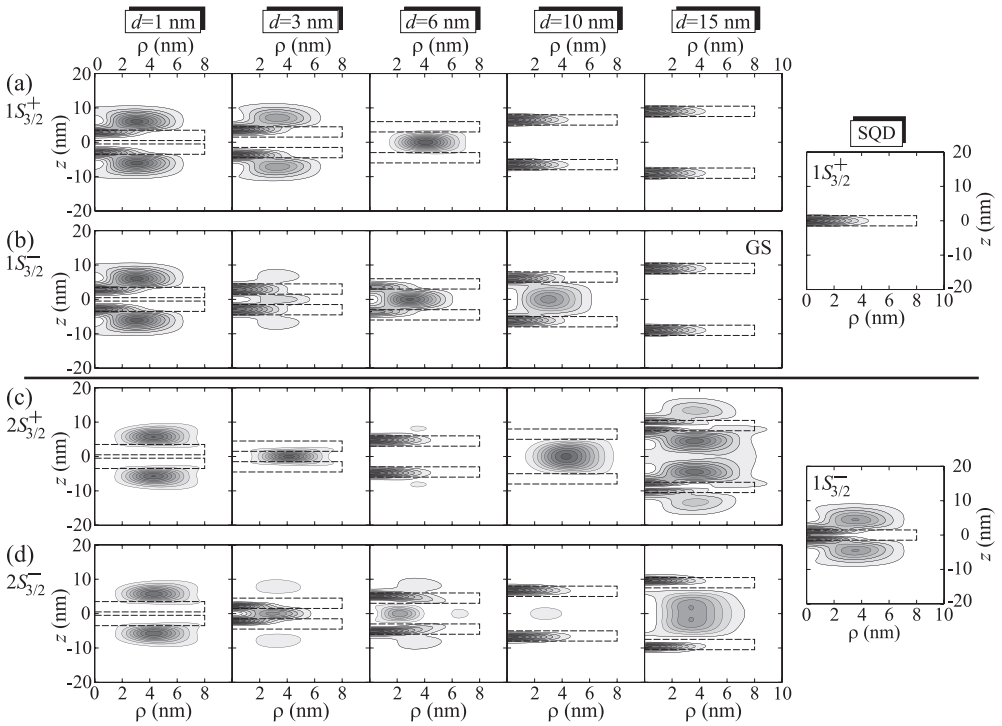

Figure 7. The contour plots of the PD distributions of the four $S_{+3/2}$ hole states as a function of the spacer thickness for $h = 3$ nm and five different values of the separation between the dots: (a) $1S^{+}_{+3/2}$, (b) $1S^{-}_{+3/2}$, (c) $2S^{+}_{+3/2}$, and (d) $2S^{-}_{+3/2}$ hole state. The thick horizontal line is used to visually separate the two doublets. The quantum dots are shown by the dashed lines. $1S^{+}_{+3/2}$ and $1S^{-}_{+3/2}$ states form a doublet stemming from the $1S^{+}_{+3/2}$ SQD state, whose PD is shown separately to the right of the panels (a) and (b). The same also applies to the states shown in the panels (c) and (d), which arise from splitting of the $1S^{-}_{+3/2}$ SQD state shown to the right of the panels (c) and (d). GS indicates that the state is the ground state of the holes.

thickness. The regions of higher PD are shown darker, the spacer thickness is indicated on the top of each column of plots, and the borders of the two dots are shown by the dashed lines. The $1S^{+}_{+3/2}$ SQD state splits into the $1S^{+}_{+3/2}$ and $1S^{-}_{+3/2}$ QDM states, and the $1S^{-}_{+3/2}$ SQD state

splits into the $2S^{+}_{+3/2}$ and $2S^{-}_{+3/2}$ states in the QDM. The values of d in the figure are chosen to illustrate hole coupling in different regimes.

Let us follow the evolution of the hole wavefunction in detail:

(i) In regime III of the hole localization (for $d \lesssim 3$ nm), it is not possible to appreciably confine the light holes in the spacer region, as shown in figures 7(a)–(d). Therefore, the $nS^{+}_{+3/2}$ and $nS^{-}_{+3/2}$ states have similar PD distributions.
(ii) The increase of the spacer thickness to 3 nm diminishes the lh clouds in the matrix above and below the stack, and brings the light holes towards the spacer region.
(iii) When d increases from 3 to 6 nm, the $1S^{+}_{+3/2}$ and $2S^{+}_{+3/2}$ states anticross, which brings the lh clouds in the $1S^{+}_{+3/2}$ state towards the spacer region, while the hh clouds, located inside the dots, are transferred to the $2S^{+}_{+3/2}$ state for $d = 6$ nm.
(iv) As figure 5(a) shows, the $1S^{+}_{+3/2}$ and $2S^{+}_{+3/2}$ states anticross for the second time near $d = 8.8$ nm, which brings back the hh-dominated clouds to the $1S^{+}_{+3/2}$ state and the lh-dominated cloud to the $2S^{+}_{+3/2}$ state.
(v) The $1S^{-}_{+3/2}$ and $2S^{-}_{+3/2}$ states anticross for the second time near $d = 12$ nm, which yields exchange of their clouds; thus the ground hole state has $S^{-}_{+3/2}$ symmetry and appears to be dominated by the heavy holes for $d = 15$ nm.
(vi) For thick spacer, the $2S^{+}_{+3/2}$ and $2S^{-}_{+3/2}$ states converge to the $1S^{-}_{+3/2}$ SQD states, which consist mainly of the even lh clouds around the two dots, and the odd hh clouds located inside the dots.

Similar PD plots for the $S_{+1/2}$ hole states, are depicted in figure 8. The two hh envelope functions are always separated by $|\Delta l_{\mathrm{h}}| = 3$; therefore the hh parts cannot *a priori* be large in the $f_{\mathrm{h}} = 1/2$ state, while for the light holes $l_{\mathrm{h}2} = 0$ and $l_{\mathrm{h}5} = 1$. Thus the PD might be composed of comparable ring-shaped and elliptically shaped clouds.

We describe the localization of the $S^{\pm}_{\pm1/2}$ holes along the same route as for the $S^{\pm}_{\pm3/2}$ states:

(i) On comparison with the $f_{\mathrm{h}} = 3/2$ states, a similar location of the holes along the z direction is found for spacers as thin as $d = 1$ nm, where the hole PD is dominated by the lh clouds located in the matrix.
(ii) Increase of d leads to anticrossing between the $1S^{+}_{+1/2}$ and $2S^{+}_{+1/2}$ states in the range 3 nm $< d <$ 4 nm (see figure 5(b)), which provides an exchange of their clouds.
(iii) For $d = 6$ nm, both the $1S^{+}_{+1/2}$ and $1S^{-}_{+1/2}$ states are located mainly between the dots, but for the latter the lh envelope function with the zero orbital momentum is s-like and even; hence its energy exceeds the energy of the former.
(iv) For 6 nm $< d <$ 10 nm, no anticrossing between the $1S^{+}_{+1/2}$ and $2S^{+}_{+1/2}$ states takes place. In this range, the PD distribution in the $1S^{+}_{+1/2}$ state is dominated by light holes.
(v) Further increase of d from 10 to 15 nm leads to an anticrossing between the $1S^{+}_{+1/2}$ and $2S^{+}_{+1/2}$ levels (see figure 5(b)), which splits the hole clouds into independent ones surrounding the two dots.
(vi) Let us briefly comment on the PD in the SQD $1S^{-}_{+1/2}$ state. It consists of the s symmetric lh clouds outside the dot, the p-like hh cloud inside the dot, and a small s-type so cloud (located around the centre of the dot), which originates from the mixing between the lh and so bands.

We can quantify the hole localization by calculating the relative contributions of the different hole bands to the total hole probability, which are plotted in figures 9(a)–(c) for the $1S^{\pm}_{+3/2}$, $1S^{\pm}_{+1/2}$, and $1P^{\pm}_{+5/2}$ states, respectively. For the $f_{\mathrm{h}} = 3/2$ states, we find that the different regimes for the hole localization are clearly visible in figure 9(a). The lh contributes over a wide

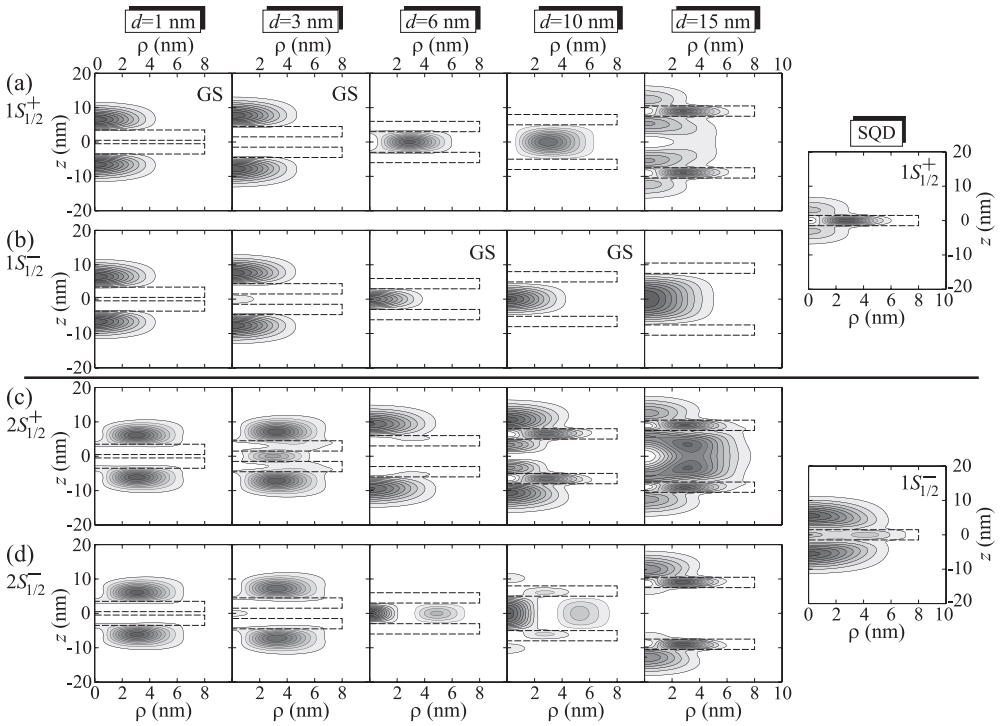

Figure 8. The same as figure 7 but now for the $S_{+1/2}$ hole states: (a) $1S^{+}_{+1/2}$, (b) $1S^{-}_{+1/2}$, (c) $2S^{+}_{+1/2}$, and (d) $2S^{-}_{+1/2}$ states. The hole clouds in the SQD $1S^{+}_{+1/2}$ and $1S^{-}_{+1/2}$ states which lead to the states in the QDM are displayed to the right of the main panels. The ground state is indicated by GS in the figures and the quantum dots are shown by the dashed lines.

range of values of d for the $1S_{+3/2}$ states of both parities, but due to the enhanced confinement of the heavy holes when d increases, the hh and lh parts in the $1S^{+}_{+3/2}$ and $1S^{-}_{+3/2}$ states cross at about $d = 8.8$ nm and near $d = 12$ nm, respectively. Therefore, these are dominantly hh in character for thick spacers. To the left of the hh–lh crossings in figure 9(a), there occur spikes at $d = 3.25$ nm, where anticrossings with other states of the same parity reconstruct the hole wavefunctions. The locations of the spikes effectively mark the borderline between regimes I and II of hole localization in the two $S_{+3/2}$ states. Similar abrupt variation, related to anticrossings near $d \approx 3$ nm, of the hh and lh parts is found in figures 9(b) and (c), where the results for the $1S^{\pm}_{+1/2}$ and $1P^{\pm}_{+5/2}$ states are shown. While the locations of the crossings between hh and lh parts are similar for the $1P^{\pm}_{+5/2}$ states, the light holes in the $S^{\pm}_{+1/2}$ state are found to dominate over a much wider range of values of d than for the $1S^{\pm}_{+3/2}$ states.

4.3. Exciton states and oscillator strength

The ground exciton state in a SQD is provided by the $1Q^{+}_{1}$ quartet. Quite generally, and similarly to the electron case (see figure 4), exciton energies exceed the SQD energies for large d (see figure 10), but the increase with decreasing d is larger and persists to lower d as compared to the electron spectra case. This implies that the behaviour of the exciton states is strongly influenced by the holes. All exciton levels exhibit doublet ordering, and, as a result of the strong anticrossings with the higher exciton states, sharper maxima in the exciton energies

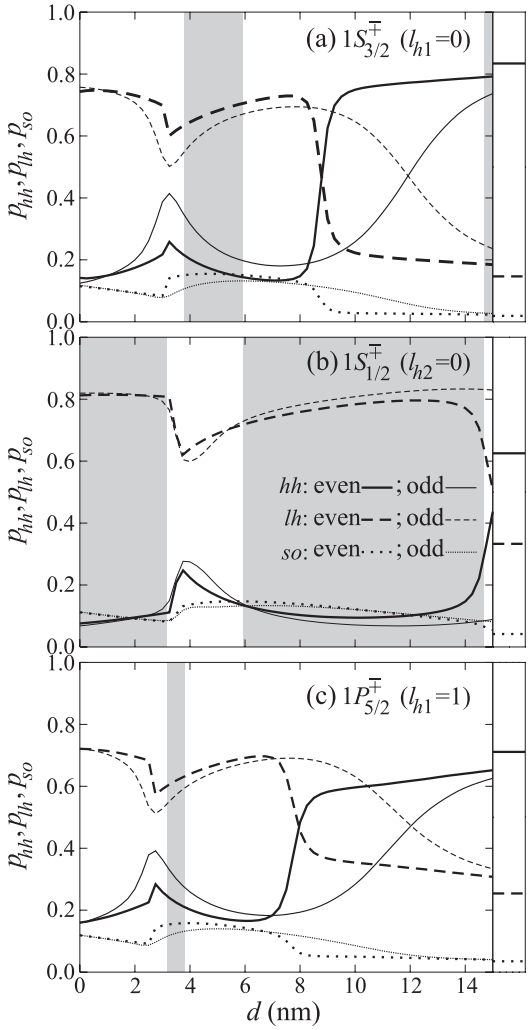

Figure 9. The contributions of the hh, lh, and so bands to the total probability in the QDM states as a function of the distance between the dots for: (a) $1S^{\pm}_{+3/2}$, (b) $1S^{\pm}_{+1/2}$, and (c) $1P^{\pm}_{+5/2}$ states. The thick (thin) solid curves denote the hh part in the even (odd) state. The lh parts in the even (odd) states are shown by the thick (thin) dashed curves. The thick (thin) dotted curves indicate the so part in the even (odd) state. In the shaded regions, the highest energy vb state of the respective f_{h} is the ground hole state. The horizontal lines in the areas to the right of the main figures are the values in the SQD. The two quantum dots in the stack are 3 nm thick.

of the ground states versus d are found for the 3 and 4 nm thick quantum dots than for $h = 2$ nm (see figure 10). Besides this, the exciton energies versus d oscillate for $h = 3$ and 4 nm, while the $1Q^{\pm}_1$ energies decrease rapidly for $h = 2$ nm and $d > 2$ nm; i.e. the ground exciton state splitting depends on d like in the antibonding state case in the strain-free system. The strain lifts the energies above the level in the SQD when d increases, and the convergence towards the values in the single quantum dot depends on the quantum-dot thickness. For $d = 15$ nm all states are close to the lowest SQD energies of the Q^{+}_1 and Q^{+}_2 symmetry, displayed as the horizontal lines in the grey areas to the right of figure 10.

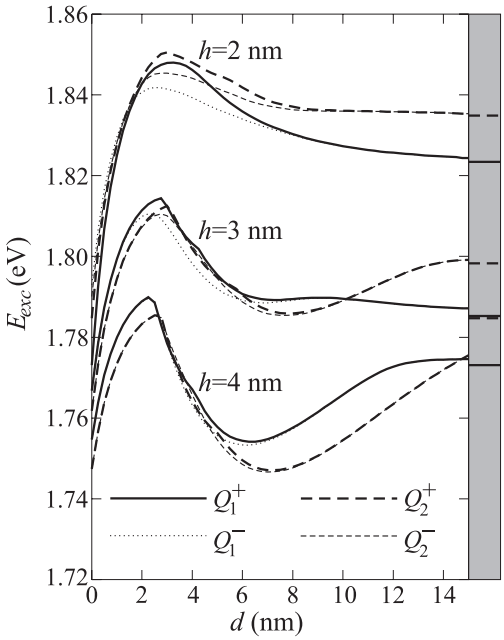

Figure 10. Energies of the $1Q_1^{\pm}$ and $1Q_2^{\pm}$ exciton quartets in QDMs, computed for $h = 2$, 3, and 4 nm, as they vary with d. Solid curves, thick dashed curves, dotted curves, and thin dashed curves denote the energies of the $1Q_1^+$, $1Q_2^+$, $1Q_1^-$, and $1Q_2^-$ quartets, respectively. The corresponding values for the SQD are displayed in the shaded region.

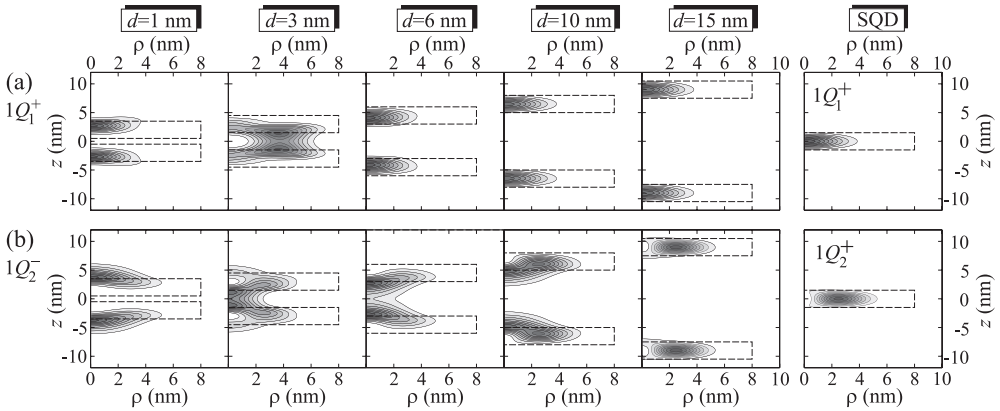

Figure 11. The two-dimensional probability density (2DPD), defined in equation (9), for the exciton quartets: (a) $1Q_1^+$ and (b) $1Q_2^-$, for $h = 3$ nm and $d = 1$, 3, 6, 10, and 15 nm. The corresponding distributions of 2DPD in the SQD excitons are shown to the right of each panel. The boundaries of the two dots are indicated by the dashed lines.

The contour plots of the exciton 2DPD shown in figure 11 shed more light on the exciton coupling in the QDM. Because of the Kramers degeneracy, the 2DPDs of the four states are equally distributed in each quartet. We show in figure 11 the 2DPD of the optically active $1Q_1^+$ and $1Q_2^-$ quartets, for the same five values of d as selected previously for the holes, i.e. for $d = 1$, 3, 6, 10, and 15 nm, and also the exciton clouds in the SQD to the right of each panel.

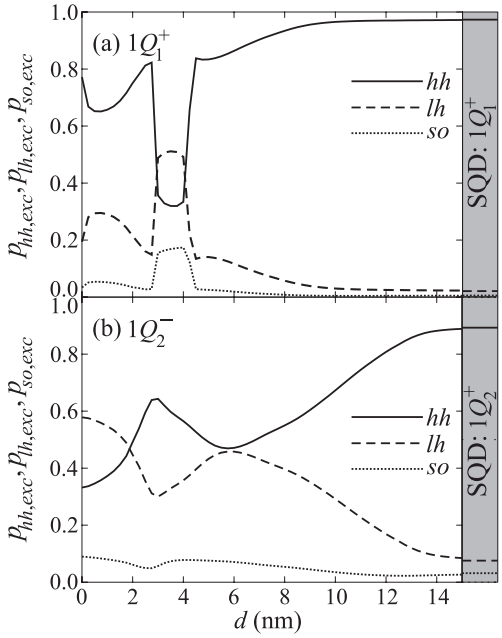

Figure 12. Relative contributions of the different hole bands to the total probability in the optically active QDM exciton quartets: (a) $1Q_1^+$ and (b) $1Q_2^-$, as a function of the spacer thickness. The solid curves indicate the hh parts, the dashed lines the lh parts, and the so parts are indicated by the dotted curves. The results for the SQD are shown by the appropriate lines in the grey areas to the right of each figure. The dot thickness is 3 nm.

In contrast to the hole states, the exciton 2DPDs do not change tremendously from left to right in figure 11, yet they exhibit a few interesting aspects:

(i) The spatial extent of 2DPDs for both exciton quartets is reduced with respect to the single-particle state case.
(ii) Like for the holes, the exciton clouds for thin spacers are located near the base of the stack.
(iii) On separating the two quantum dots, the 2DPDs of both states are relocated to the spacer.
(iv) The peaks of the $1Q_1^+$ 2DPD are located on the z axis, and their localization in the dots indicates that they are mostly hh-like for thick spacers, while the contribution of the light holes located outside the dots is larger for thin spacers.
(v) The 2DPD of the $1Q_2^-$ quartet has a ring configuration for $d = 15$ nm, with the peaks located inside the dots.
(vi) The 2DPDs for both quartets are for $d = 15$ nm already converged to the case for uncoupled dots in the stack. One should note here that the $1Q_2^-$ quartet originates from the $1Q_2^+$ SQD states.

Parts of the lowest energy exciton states which belong to the different bands vary considerably with the thickness of the spacer, as figures 12(a) and (b) show for the $1Q_1^+$ and $1Q_2^-$ exciton quartets, which exhibit the largest optical activity for $x(y)$ and z polarized light, respectively. In accordance with the composition of the hole states in the SQD, the heavy holes give the largest contribution in both exciton quartets depicted in figure 12, whereas lh and so parts contribute much less. Thinning the spacer increases the mixing of the lh and so bands in the $1Q_1^+$ exciton states. The transition from the hh-dominated to the lh-dominated

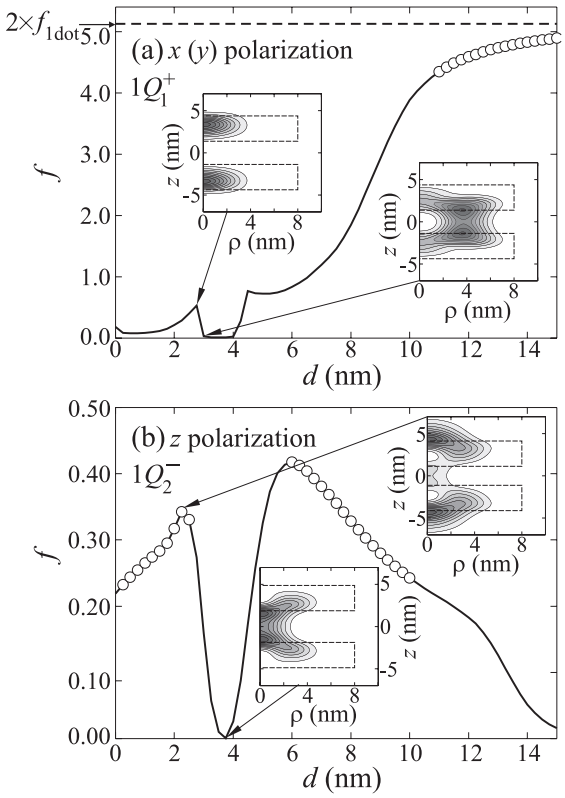

Figure 13. (a) The oscillator strength for x (y) polarized light and the $1Q_1^+$ quartet in the QDM composed of 3 nm thick quantum dots. The result for two SQDs is shown by the dashed line. The two insets show the 2DPD distributions for $d = 2.5$ and 2.75 nm. (b) The oscillator strength for z polarized light and the $1Q_2^-$ quartet. The decrease of the oscillator strength is caused by the redistribution of the exciton 2DPD, as displayed in the insets. The ranges where the displayed quartets are the ground exciton state are shown by the circles (○).

exciton states takes place in region II of the hole localization, where the hole wavefunctions relocate from the spacer to the matrix, which affects the exciton states (see figure 11).

The oscillator strength also exhibits a strong variation with d, as depicted in figure 13(a) for the $1Q_1^+$ exciton quartet and x (or y) polarized light, and figure 13(b) for the $1Q_2^-$ exciton quartet and z polarized light. The $1Q_2^-$ quartet also exhibits optical activity for x (or y) polarized light, but the peak of its oscillator strength is two orders of magnitude lower as compared to the $1Q_1^+$ quartet one, and therefore it is not shown in figure 13(a). Equations (15*a*)–(15*f*) show that the oscillator strength for x and y polarized light depends on the envelope functions for all three valence bands, while for z polarized light non-zero weight is given only to the lh and so bands. As shown in the grey areas of figure 12, the hh-dominated composition of the SQD states offers favourable conditions for the transitions induced by x (y) polarized light, while rather low lh and so parts reduce the oscillator strength for z polarized light. Hence, different values of the oscillator strength for the two quartets are found for the thick spacers. When the two dots in the molecule are far from each other, they behave as independent quantum systems; therefore the oscillator strength in figure 13(a) tends to twice the SQD result with increasing d, which is also the case for the $1Q_2^-$ quartet, but the value in the SQD is rather low. Due to the increase of the lh part, the oscillator strength for the $1Q_1^+$ state decreases

smoothly when the spacer becomes thinner. Decrease of the relevant hh envelope function for the spin up excitons due to anticrossings with the $2Q_1^+$ quartet, however, abruptly depletes the oscillator strength in the range 3 nm $< d <$ 4 nm. The insets in figure 13 show a relationship between the decrease of the oscillator strength and the change of the 2DPD distribution. For the $1Q_2^-$ exciton quartet shown in figure 13(b), no abrupt variation of the oscillator strength for z polarized light is found, yet the selection rule and the variation of the different parts cleave the oscillator strength into two parts. Because of the smaller lh and so parts, an oscillator strength in the peaks an order of magnitude lower is computed for the $1Q_2^-$ state and z polarized light, as compared with that for the $1Q_1^+$ state and x (y) polarized light. However, both exciton quartets analysed are the ground state of the system in restricted ranges of d, as indicated by the circles in figure 13.

5. Conclusion

The exciton states and the oscillator strength in quantum-dot molecules composed of two InP/InGaP quantum discs were computed as a function of the thickness of the InGaP spacer. We assumed that the two dots had the same size, and numerical calculations were performed for a few values of the disc thickness. Our results showed that the ground state energies in the different electron shells of the QDM increase to above the energy in the single quantum dot. A similar behaviour was found for the holes, but band mixing becomes more effective on relocating holes from the spacer to the dots, and consequently the hole energy levels exhibit more extrema with varying d. Our results demonstrate type-I localization for the heavy holes, and type-II localization for the light holes. The light holes are mainly responsible for the coupling of the hole states. For a thin spacer, the light holes relocate to the large regions in the matrix, which pairs the energy levels in doublets in a much more effective way than for large spacer thicknesses. The peculiar behaviour of the hole states affects the exciton energies, which exhibit blue shifts with respect to the energy in a single quantum dot. Also, the exciton energies are found to oscillate when d varies, which is a result of the strong variation of the hole energy levels when d varies. The oscillator strength for exciton recombination is subject to strong variations with the distance between the dots. As a matter of fact, due to the decrease of the hh parts in the $1Q_1^+$ exciton quartet, which shows the largest optical activity among all exciton states explored, the oscillator strength for x (or y) polarized light almost vanishes in a certain range of d. This change effectively causes the bright exciton of the single quantum dot to revert to being a dark exciton in the quantum-dot molecule.

Acknowledgments

This work was supported by the European Commission GROWTH programme NANOMAT project, Contract No G5RD-CT-2001-00545, the University of Antwerp (GOA and VIS), the Belgian Science Policy, and the Serbian Ministry of Science. We would like to acknowledge fruitful discussions with B Partoens, P Hawrylak, and M Hayne.

References

[1] Bimberg D, Grundmann M and Ledentsov N N 1999 *Quantum Dot Heterostructures* (Chichester: Wiley)
[2] Jacak L, Hawrylak P and Wójs A 1998 *Quantum Dots* (Berlin: Springer)
[3] Rontani M, Amaha S, Muraki K, Manghi F, Molinari E, Tarucha S and Austing D G 2004 *Phys. Rev.* B **69** 085327
[4] Belluchi D, Rontani M, Troiani F, Goldoni G and Molinari E 2004 *Phys. Rev.* B **69** 201308(R)

[5] Tadić M, Peeters F M and Janssens K L 2002 *Phys. Rev.* B **65** 165333
[6] Tadić M, Peeters F M, Janssens K L, Korkusiński M and Hawrylak P 2002 *J. Appl. Phys.* **92** 5819
[7] Pryor C, Pistol M-E and Samuelson L 1997 *Phys. Rev.* B **56** 10404
[8] Stier O, Grundmann M and Bimberg D 1999 *Phys. Rev.* B **59** 5688
[9] Schliwa A, Stier O, Heitz R, Grundmann M and Bimberg D 2001 *Phys. Status Solidi* b **224** 405
[10] Wang L W 2000 *Phys. Rev.* B **61** 7241
[11] Kolokov K I, Li J and Ning C Z 2003 *Phys. Rev.* B **68** 161308
[12] Pedersen F B and Chang Y-C 1996 *Phys. Rev.* B **53** 1507
[13] Efros Al L, Rosen M, Kuno M, Nirmal M, Norris D J and Bawendi M 1996 *Phys. Rev.* B **54** 4843
[14] Vurgaftman I, Meyer J R and Ram-Mohan L R 2001 *J. Appl. Phys.* **89** 5815
[15] Fonseca L R, Jimenez J L and Leburton J P 1998 *Phys. Rev.* B **58** 9955
[16] Pryor C 1998 *Phys. Rev. Lett.* **80** 3579